

# Extensive degeneracy, Coulomb phase and magnetic monopoles in artificial square ice

Yann Perrin<sup>1,2</sup>, Benjamin Canals<sup>1,2</sup> & Nicolas Rougemaille<sup>1,2</sup>

Artificial spin-ice systems are lithographically patterned arrangements of interacting magnetic nanostructures that were introduced as way of investigating the effects of geometric frustration in a controlled manner<sup>1–4</sup>. This approach has enabled unconventional states of matter to be visualized directly in real space<sup>5–18</sup>, and has triggered research at the frontier between nanomagnetism, statistical thermodynamics and condensed matter physics. Despite efforts to create an artificial realization of the square-ice model—a two-dimensional geometrically frustrated spin-ice system defined on a square lattice—no simple geometry based on arrays of nanomagnets has successfully captured the macroscopically degenerate ground-state manifold of the model<sup>19</sup>. Instead, square lattices of nanomagnets are characterized by a magnetically ordered ground state that consists of local loop configurations with alternating chirality<sup>1,20–26</sup>. Here we show that all of the characteristics of the square-ice model are observed in an artificial square-ice system that consists of two sublattices of nanomagnets that are vertically separated by a small distance. The spin configurations we image after demagnetizing our arrays reveal unambiguous signatures of a Coulomb phase and algebraic spin-spin correlations, which are characterized by the presence of ‘pinch’ points in the associated magnetic structure factor. Local excitations—the classical analogues of magnetic monopoles<sup>27</sup>—are free to evolve in an extensively degenerate, divergence-free vacuum. We thus provide a protocol that could be used to investigate collective magnetic phenomena, including Coulomb phases<sup>28</sup> and the physics of ice-like materials.

To recover the true degeneracy associated with the square-ice model, we fabricated a series of artificial square-ice systems inspired by a previous theoretical proposition<sup>29</sup>. The main idea behind that proposition is to reduce the coupling strength between perpendicularly oriented nanomagnets ( $J_1$ ) while keeping the coupling strength between collinear nanomagnets ( $J_2$ ) unchanged by vertically shifting one of the two sublattices of the square array (Fig. 1a). Such a height offset  $h$  makes it possible to finely tune the  $J_1/J_2$  ratio. If  $h=0$ , then the system is a conventional artificial square-ice system, characterized by  $J_1 > J_2$  and a magnetically ordered ground state (Fig. 1b). If  $h$  is continuously increased, then  $J_1$  can become infinitively small compared to  $J_2$  until a situation is reached where the horizontal and vertical lines of the square lattice are magnetically decoupled ( $J_1=0$ ; Fig. 1c). Therefore, there is necessarily a critical height offset  $h_c$  at which the two coupling coefficients  $J_1$  and  $J_2$  are equal (Fig. 1d). On the basis of a dumbbell description of the nanomagnets, it was found<sup>29</sup> that  $h_c = 0.207a$  for  $l/a = 0.7$ , where  $l$  is the length of the nanomagnets and  $a$  is the lattice parameter. A critical height offset of  $h_c = 0.27a$  was calculated<sup>30</sup> by incorporating dipolar interactions over the entire volume of uniformly magnetized nanomagnets. However, both of these approaches neglected key experimental ingredients: the geometric properties and the micromagnetic nature of the nanomagnets were not taken into account. Here, we determine  $h_c$  from a set of micromagnetic simulations that describe the real shape and internal micromagnetic configuration of the

nanomagnets used experimentally (Methods). The main result of our calculation is that  $h_c$  strongly depends on the gap left between neighbouring magnetic elements, and is qualitatively similar to the estimate deduced from the dumbbell description (Fig. 1e and Extended Data Fig. 1), but quantitatively very different.

To recover the degeneracy of the square-ice model, we need to lithographically pattern arrays of nanomagnets in which the third dimension now plays a key part, extending artificial spin-ice systems from two to three dimensions. This additional dimension makes the fabrication and imaging of spin-ice architectures much more challenging. Our shifted artificial square-ice systems were fabricated using a two-step electron-beam lithography process (Methods and Extended Data Fig. 2). The first step is dedicated to the design of non-magnetic bases that are used to lift one sublattice of nanomagnets. The thickness of the bases determines the final height offset  $h$  (the base thicknesses used here are 60 nm, 80 nm and 100 nm). The second step

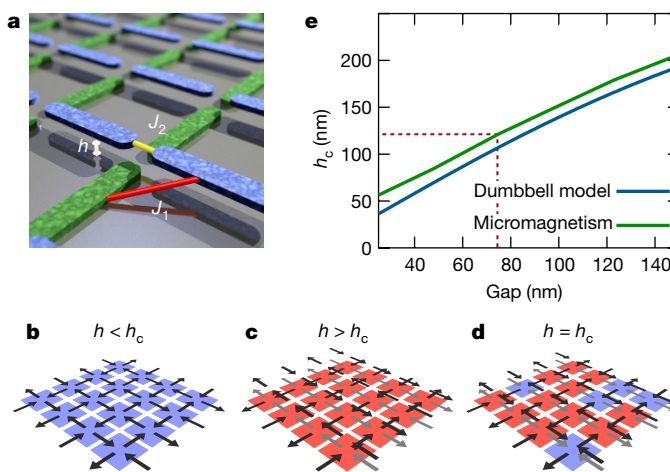


**Figure 1 | Role of the nearest-neighbour coupling strength.** **a**, Schematic of artificial square ice (inspired by ref. 29) in which one of the two sublattices (blue) is shifted vertically by a height offset  $h$  above the other (green). The nearest-neighbour coupling strengths between orthogonal ( $J_1$ ) and collinear ( $J_2$ ) nanomagnets are indicated in red and yellow, respectively. **b–d**, Ground states of the models associated with the conditions  $J_1 > J_2$  ( $h < h_c$ ; **b**),  $J_1 < J_2$  ( $h > h_c$ ; **c**) and  $J_1 = J_2$  ( $h = h_c$ ; **d**). Blue and red squares correspond to type-I and -II vertices, respectively. Black arrows indicate the local spin directions. Grey arrows represent the projection of the spin directions of the shifted sublattice on the  $h=0$  plane. **e**, Plot showing the critical height offset  $h_c$  that is required to recover ice-like physics, as a function of the gap separating nearest-neighbour nanomagnets. Results derived from micromagnetic simulations (green) and from a dumbbell description (blue) of the nanomagnets are compared. The red dashed line indicates the value of  $h_c$  that we expect to observe in our experiments, given that the gap between nearest-neighbour nanomagnets is 75 nm. The length, width and thickness of our nanomagnets are 500 nm, 100 nm and 30 nm, respectively. More details are provided in the Methods.

consists of depositing the nanomagnets on a square lattice in such a way that one sublattice is grown atop the non-magnetic bases and the other is grown on the substrate. On each sample, a reference square lattice with  $h = 0$  is patterned for direct comparison with the shifted arrays. Magnetic images were obtained using magnetic force microscopy (Fig. 2a) after demagnetizing the arrays in an in-plane oscillating magnetic field with slowly decaying amplitude (Methods). All of the arrays were demagnetized simultaneously to ensure identical field history between samples.

The three shifted arrays we studied were demagnetized four times to improve the statistics and to test the reproducibility of the experimental observations, and we systematically imaged the reference array ( $h = 0$ ) present on each sample to check the efficiency of the field demagnetization protocol. For these 12 realizations, the reference arrays were always found in a magnetic configuration close to the ordered antiferromagnetic ground state (Fig. 1b). A typical magnetic state is shown in Fig. 2b, in which a domain boundary separating two anti-phase domains is observed. Consequently, type-I vertices are present everywhere, except in the domain wall formed by type-II vertices (for definitions of type-I and -II vertices, see the inset of Fig. 1a). Our demagnetization protocol is therefore efficient and brings the system into a low-energy manifold, with large patches of the ground-state configuration, similar to what is found in thermally active artificial spin ices<sup>10,21,24–26</sup>. For the reference arrays, the density of type-I, -II, -III and -IV vertices are, on average, 86%, 12.5%, 1.5% and 0%, respectively (Fig. 2c; type-III (-IV) vertices refer to vertices with three (four) in or three (four) out spin configurations<sup>1</sup>), and the mean size of type-I domains is about 87 vertices. Consequently, the residual magnetization is low, typically 3% in both the vertical and horizontal directions. The computed magnetic structure factor (Methods and Extended Data Fig. 3), averaged over the 12 different reference arrays, shows clear magnetic Bragg peaks located at the corners of the Brillouin zone (Fig. 3a).

Figure 2c shows the variation in vertex density  $\rho$  when  $h$  is increased, revealing a clear trend: the density of type-I vertices continuously decreases whereas the density of type-II vertices increases. For  $h = 60$  nm, the physics is essentially unchanged from the  $h = 0$  case: type-I vertices are the most prevalent and form patches of the antiferromagnetic ground state, although the average size of the ordered domains decreases to 15 vertices—6 times smaller than for the reference arrays. The corresponding magnetic structure factor shows a spreading of the magnetic Bragg peaks associated with antiferromagnetic ordering, but the peaks remain located at the corners of the Brillouin zone (Fig. 3b). This result is consistent with the predictions from micromagnetic simulations (Fig. 1e), which indicate that the ground state is expected to be the antiferromagnetic ordered configuration when  $h = 60$  nm.

For  $h = 80$  nm, the population of type-II vertices (52%) becomes higher than that of type-I vertices (39%); type-II patches start to form and the spatial extent of type-I domains is further reduced. The magnetic Bragg peaks in the magnetic structure factor have almost disappeared, which is an indication that the spin configurations have started to be disordered. If the background intensity in the magnetic structure factor becomes more diffuse, then it develops a structure with geometric features that resemble those expected from the square-ice model (Fig. 3c, e and Methods). This result is consistent with the micromagnetic simulations: although the ground state is expected to be the antiferromagnetic ordered configuration, the magnetic configuration is disordered after demagnetizing the array, as  $h$  approaches  $h_c$  ( $J_1$  starts to compare with  $J_2$ ).

The similarity to the square-ice model becomes more evident for  $h = 100$  nm (Fig. 3d, e). Contrary to all previous results, which demonstrate that square lattices of nanomagnets are magnetically ordered in their low-energy manifold, we show that our artificial square ice is highly disordered. The magnetic Bragg peaks in the magnetic structure factor have totally disappeared for  $h = 100$  nm and the diffuse

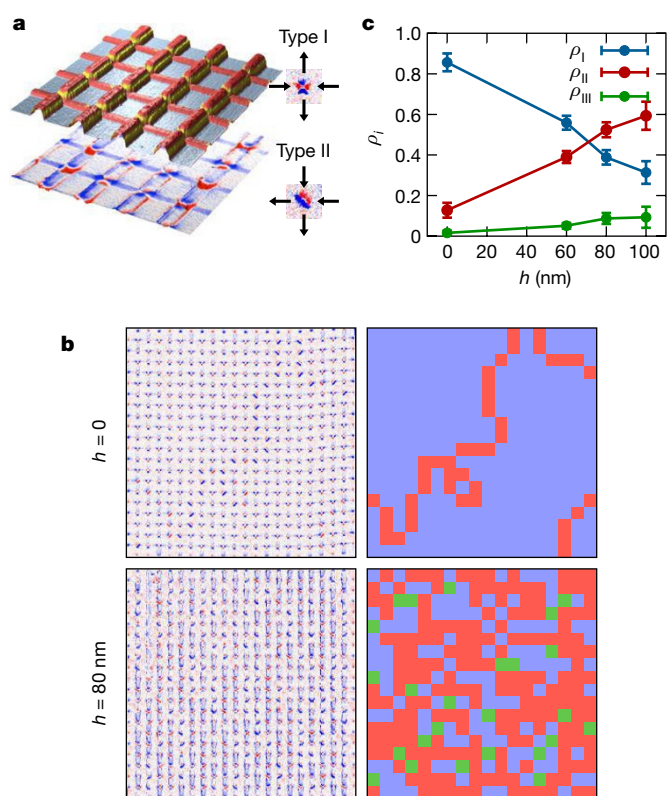


**Figure 2 | Experimental results.** **a**, Topography (atomic force microscopy; top) and magnetic (magnetic force microscopy; bottom) images of our artificial realization of the square-ice model. In the topography image, the nanomagnets appear red, the bases are yellow and the substrate is grey. In the magnetic image, the magnetic contrast appears in blue and red for negative and positive magnetic charges, respectively. Typical contrasts obtained on type-I and -II vertices are shown in the inset. Type-I (-II) vertices correspond to local two-in/two-out spin configurations carrying zero (net) magnetic moment. **b**, Magnetic images (raw data on the left and the corresponding analysis on the right) for a height offset of  $h = 0$  (top) and  $h = 80$  nm (bottom). For  $h = 0$ , most of the vertices are type-I (blue), and a domain boundary separating anti-phase domains is clearly visible (type-II vertices are shown in red). For  $h = 80$  nm, the magnetic state appears disordered; type-III vertices are coloured in green. **c**, Analysis of the vertex density of type- $i$  vertices  $\rho_i$  as a function of the height offset  $h$ . The points represent the mean and the error bars represent the standard deviation calculated from the four demagnetizations.

background is strongly structured. However, on the basis of the micromagnetic simulations presented above, the ground state of artificial square ice with  $h = 100$  nm is expected to be ordered. We interpret this difference between observation and prediction as a consequence of the kinetics associated with the spin dynamics when the sample is demagnetized under a rotating magnetic field. During the demagnetization protocol, spins are reversed via an avalanche process that favours the formation of straight lines (Methods and Supplementary Videos 1 and 2). Type-II vertices are then stabilized by the external magnetic field at the expense of type-I vertices, even though type-I vertices have a slightly lower energy. In other words, our protocol shifts the critical value  $h_c$ , at which the transition to the disordered phase is expected.

Our square ice exhibits all of the characteristics of a dipolar algebraic spin liquid. In such a spin liquid, there are locations in reciprocal space where the magnetic structure factor behaves non-analytically and has the shape of a pinch point. These pinch points are visible in our experimental map (Fig. 3d, circle) and are indicative of a Coulomb phase<sup>28</sup>. To gain more insight into the observed physics, we quantitatively compare, on the experimental and theoretical maps,  $q$ -scans of the magnetic structure factor along two orthogonal lines passing through these pinch

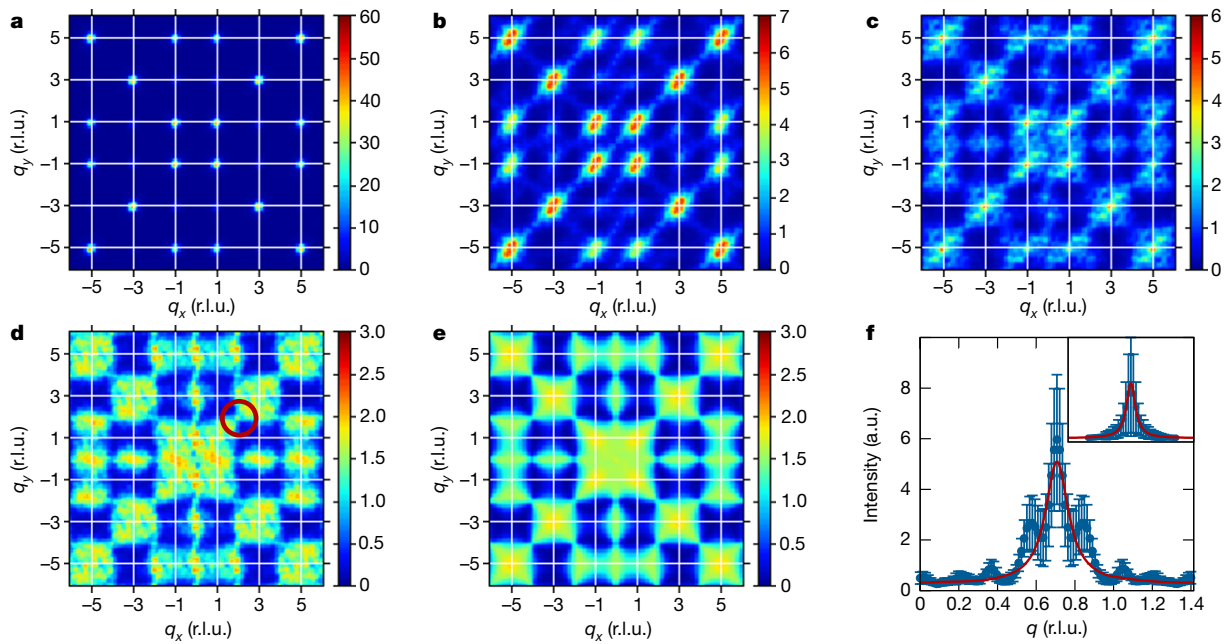


**Figure 3 | Magnetic structure factors and pinch-point analysis.**

**a–d**, Magnetic structure factors deduced from the experimental images for  $h = 0$  (**a**),  $h = 60$  nm (**b**),  $h = 80$  nm (**c**) and  $h = 100$  nm (**d**). The colour scale refers to the intensity at a given point ( $q_x, q_y$ ) of reciprocal space. **e**, Computed magnetic structure factor averaged over 1,000 random, decorrelated spin configurations that satisfy the ice rule (Methods). **f**, Experimental (main plot) and theoretical (inset) intensity profiles

across the pinch point highlighted by a red circle in **d**. The points represent the mean and the error bars represent the standard deviation calculated from the four demagnetizations for the experimental data and the 1,000 random ice-rule configurations for the theoretical data. The red curves are single-peaked Lorentzian fits of the pinch points. The  $q$  axis corresponds to a scan from  $(3/2, 5/2)$  to  $(5/2, 3/2)$  in reciprocal space. r.l.u., reciprocal lattice unit; a.u., arbitrary units.

points (Methods, Extended Data Figs 4 and 5 and Extended Data Table 1). Whereas the theoretical scan reveals a sharp peak associated with a correlation length of  $\xi_{\text{theo}} = 5.2a \pm 4\%$ , the experimental scan displays a broader peak associated with a shorter correlation length of  $\xi_{\text{exp}} = 4.4a \pm 12\%$ . The broader peaks indicate the presence of local excitations, that is, a finite density of classical monopoles within a Coulomb phase.

Experimentally, we observe a similar density of  $+2$  and  $-2$  monopoles for all of the arrays (although they do not systematically obey charge neutrality owing to their finite size), with the density increasing as we retrieve the degeneracy of the square-ice model (see  $h$  dependence of type-III vertices in Fig. 2c). The variation in the monopole density we measure is not random and appears to be robust when comparing successive demagnetization protocols. The

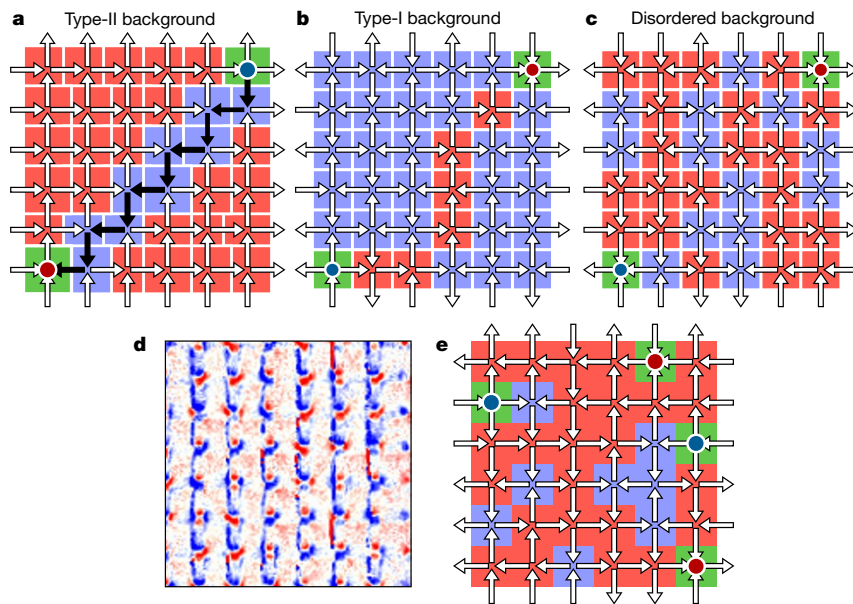


**Figure 4 | Magnetic monopoles in square-ice systems.** **a–c**, Monopole/anti-monopole pair (red and blue circles) in a magnetically saturated background (type-II background; **a**), in the antiferromagnetic ground state (type-I background; **b**) and within a disordered manifold (disordered background; **c**). Blue, red and green squares indicate type-I, -II and -III

vertices, respectively. The black arrows in **a** illustrate a chain of reversed spins. **d**, Experimental spin configurations for  $h = 100$  nm showing two pairs of oppositely charged monopoles. **e**, Analysis of the configuration in **d**. Monopoles appear as red and blue circles on top of a green square.



densities are fairly high when approaching the spin-liquid phase (Fig. 2c), meaning that we do not bring the system into its massively degenerate ground-state manifold. Instead, the imaged spin configurations are characteristic of excited states embedded within a Coulomb phase. The monopoles that we observe in our arrays differ substantially from those that have previously been visualized in artificial square ices<sup>1,20–26</sup>. All of the monopoles reported so far are high-energy local configurations evolving in an uncharged, but magnetically ordered, vacuum (Fig. 4a, b), characterized by a magnetic structure factor that contains only magnetic Bragg peaks (Methods).

Our system has very distinct behaviour: the monopoles we observe are free to move into a spin-liquid state, that is, a massively degenerate, disordered low-energy manifold (Fig. 4c). They are therefore particle-like objects present in a diffuse but structured magnetic structure factor, free of any Bragg peaks (Fig. 3d). An example experimental configuration is shown in Fig. 4d and is schematized in Fig. 4e. Two pairs of oppositely charged monopoles are present in this disordered magnetic configuration containing type-I and -II vertices. It is not possible to determine the path that these monopoles have followed during the demagnetization process, because the trace of reversed spins (often referred to as a Dirac string) has been erased by the magnetic disorder. This is in contrast to the aforementioned cases for which monopoles evolve within an ordered spin configuration and for which the influence of the field or temperature can be unambiguously visualized (Fig. 4a, b). Here, there is no way of knowing the trajectory of the magnetic monopoles and, consequently, it is not even possible to pair two oppositely charged monopoles.

This result raises interesting, crucial questions. We envision that, if similar artificial, shifted square-ice systems could be made thermally active, the dynamics of these de-confined, interacting quasi-particles could be investigated in real space and time. We then wonder whether a typical distance between oppositely charged monopoles would be established at thermodynamic equilibrium and whether this distance could be linked to the correlation length that was deduced from the analysis of the width of the pinch point (Extended Data Fig. 6 and Methods). It would also be interesting to study how these quasi-particles nucleate, propagate and annihilate with their anti-particle, and to directly observe how their interactions affect the disordered background.

We have shown that shifted magnetic square lattices offer the possibility to tune the nearest-neighbour coupling strength and, in particular, to experimentally realize the seminal square-ice model. The fabrication of thermally active, shifted square ice in the future would enable the thermodynamics and dynamics of the low-energy manifolds and the recombination of their topological excitations to be investigated (Methods). Finally, our work demonstrates that artificial loop models, such as the square-ice model, are not beyond reach, thanks to lithography engineering. These models have numerous extensions in very different fields of research, including polymer physics, topological quantum computing, self-avoiding random walks and Schramm–Loewner evolution. Implementing loop models is therefore of broad interest in physics and chemistry, and our contribution illustrates that magnetic versions of these loop models are experimentally accessible.

**Online Content** Methods, along with any additional Extended Data display items and Source Data, are available in the online version of the paper; references unique to these sections appear only in the online paper.

**Received 28 July; accepted 12 October 2016.**

**Published online 28 November 2016.**

- Wang, R. F. *et al.* Artificial spin ice in a geometrically frustrated lattice of nanoscale ferromagnetic islands. *Nature* **439**, 303–306 (2006).
- Nisoli, C., Moessner, R. & Schiffer, P. Artificial spin ice: designing and imaging magnetic frustration. *Rev. Mod. Phys.* **85**, 1473–1490 (2013).
- Heyderman, L. J. & Stamps, R. L. Artificial ferroic systems: novel functionality from structure, interactions and dynamics. *J. Phys. Condens. Matter* **25**, 363201 (2013).

- Cummings, J., Heyderman, L. J., Marrows, C. H. & Stamps, R. L. Focus on artificial frustrated systems. *New J. Phys.* **16**, 075016 (2014).
- Ladak, S., Read, D. E., Perkins, G. K., Cohen, L. F. & Branford, W. R. Direct observation of magnetic monopole defects in an artificial spin-ice system. *Nat. Phys.* **6**, 359–363 (2010).
- Mengotti, E. *et al.* Real-space observation of emergent magnetic monopoles and associated Dirac strings in artificial kagome spin ice. *Nat. Phys.* **7**, 68–74 (2011).
- Rougemaille, N. *et al.* Artificial kagome arrays of nanomagnets: a frozen dipolar spin ice. *Phys. Rev. Lett.* **106**, 057209 (2011).
- Zhang, S. *et al.* Crystallites of magnetic charges in artificial spin ice. *Nature* **500**, 553–557 (2013).
- Montaigne, F. *et al.* Size distribution of magnetic charge domains in thermally activated but out-of-equilibrium artificial spin ice. *Sci. Rep.* **4**, 5702 (2014).
- Drisko, J., Daunheimer, S. & Cummings, J. FePd<sub>3</sub> as a material for studying thermally active artificial spin ice systems. *Phys. Rev. B* **91**, 224406 (2015).
- Anghinolfi, L. *et al.* Thermodynamic phase transitions in a frustrated magnetic metamaterial. *Nat. Commun.* **6**, 8278 (2015).
- Chioar, I. A. *et al.* Kinetic pathways to the magnetic charge crystal in artificial dipolar spin ice. *Phys. Rev. B* **90**, 220407(R) (2014).
- Zhang, S. *et al.* Perpendicular magnetization and generic realization of the Ising model in artificial spin ice. *Phys. Rev. Lett.* **109**, 087201 (2012).
- Chioar, I. A. *et al.* Nonuniversality of artificial frustrated spin systems. *Phys. Rev. B* **90**, 064411 (2014).
- Chioar, I. A., Rougemaille, N. & Canals, B. Ground-state candidate for the dipolar kagome Ising antiferromagnet. *Phys. Rev. B* **93**, 214410 (2016).
- Gilbert, I. *et al.* Emergent ice rule and magnetic charge screening from vertex frustration in artificial spin ice. *Nat. Phys.* **10**, 670–675 (2014).
- Brooks-Bartlett, M. E., Banks, S. T., Jaubert, L. D. C., Harman-Clarke, A. & Holdsworth, P. C. W. Magnetic-moment fragmentation and monopole crystallization. *Phys. Rev. X* **4**, 011007 (2014).
- Canals, B. *et al.* Fragmentation of magnetism in artificial kagome dipolar spin ice. *Nat. Commun.* **7**, 11446 (2016).
- Lieb, E. H. Residual entropy of square ice. *Phys. Rev.* **162**, 162–172 (1967).
- Nisoli, C. *et al.* Effective temperature in an interacting vertex system: theory and experiment on artificial spin ice. *Phys. Rev. Lett.* **105**, 047205 (2010).
- Morgan, J. P., Stein, A., Langridge, S. & Marrows, C. H. Thermal ground-state ordering and elementary excitations in artificial magnetic square ice. *Nat. Phys.* **7**, 75–79 (2011).
- Budrikis, Z., Politi, P. & Stamps, R. L. Diversity enabling equilibration: disorder and the ground state in artificial spin ice. *Phys. Rev. Lett.* **107**, 217204 (2011).
- Budrikis, Z. *et al.* Domain dynamics and fluctuations in artificial square ice at finite temperatures. *New J. Phys.* **14**, 035014 (2012).
- Farhan, A. *et al.* Direct observation of thermal relaxation in artificial spin ice. *Phys. Rev. Lett.* **111**, 057204 (2013).
- Porro, J. M., Bedoya-Pinto, A., Berger, A. & Vavassori, P. Exploring thermally induced states in square artificial spin-ice arrays. *New J. Phys.* **15**, 055012 (2013).
- Kapaklis, V. *et al.* Thermal fluctuations in artificial spin ice. *Nat. Nanotechnol.* **9**, 514–519 (2014).
- Castelnovo, C., Moessner, R. & Sondhi, S. L. Magnetic monopoles in spin ice. *Nature* **451**, 42–45 (2008).
- Henley, C. L. The “Coulomb phase” in frustrated systems. *Annu. Rev. Condens. Matter Phys.* **1**, 179–210 (2010).
- Möller, G. & Moessner, R. Artificial square ice and related dipolar nanoarrays. *Phys. Rev. Lett.* **96**, 237202 (2006).
- Thonig, D., Reißaus, S., Mertig, I. & Henk, J. Thermal string excitations in artificial spin-ice square dipolar arrays. *J. Phys. Condens. Matter* **26**, 266006 (2014).

**Supplementary Information** is available in the online version of the paper.

**Acknowledgements** This work was supported by the Agence Nationale de la Recherche through project number ANR12-BS04-009 ‘Frustrated’. We acknowledge support from the Nanofab team at the Institut NÉEL and thank S. Le-Denmat and O. Fruchart for technical help during atomic force microscope and magnetic force microscope measurements.

**Author Contributions** B.C. and N.R. conceived the project. Y.P. was in charge of the sample fabrication and characterization, the magnetic imaging measurements and the analysis of the data. All authors contributed to the preparation of the manuscript.

**Author Information** Reprints and permissions information is available at [www.nature.com/reprints](http://www.nature.com/reprints). The authors declare no competing financial interests. Readers are welcome to comment on the online version of the paper. Correspondence and requests for materials should be addressed to N.R. ([nicolas.rougemaille@neel.cnrs.fr](mailto:nicolas.rougemaille@neel.cnrs.fr)).

**Reviewer Information** Nature thanks C. Nisoli, A. Ramirez and the other anonymous reviewer(s) for their contribution to the peer review of this work.

## METHODS

**Micromagnetic simulations.** Micromagnetic effects have been shown to play an important part in artificial spin ices, for example by modifying the coupling strength between neighbouring elements<sup>7</sup>, by inducing chirality<sup>31</sup> and by controlling magnetization reversal processes<sup>32</sup>. Our micromagnetic simulations are based on a finite-difference approach whereby the system is discretized into rectangular cells. We used the three-dimensional solver of the OOMMF free software from the National Institute for Standards and Technology (NIST)<sup>33</sup>. We computed the four energy levels  $E_i$  ( $i \in \{1, 2, 3, 4\}$ ) of an isolated square vertex composed of four permalloy nanomagnets in magnetostatic interaction. The nanomagnets have dimensions of  $500 \text{ nm} \times 100 \text{ nm} \times 30 \text{ nm}$ . The gap  $g$  between the nanomagnets is defined as the distance between the extremities of the nanomagnet and the centre of the vertex. In all calculations, the exchange stiffness is set to  $10 \text{ pJ m}^{-1}$ , the magnetocrystalline anisotropy is neglected, spontaneous magnetization  $M_s$  is  $8 \times 10^5 \text{ A m}^{-1}$  (1.0 T) and the damping coefficient is set to 1 to speed up convergence. Given that the volume of a nanomagnet is  $1.44 \times 10^{-21} \text{ m}^3$ , our nanomagnets carry a magnetic moment of about  $\mu = 11.5 \times 10^{-16} \text{ A m}^2$ . To limit the influence of numerical roughness, the mesh size was reduced to  $3 \text{ nm} \times 3 \text{ nm} \times 15 \text{ nm}$ . No qualitative difference was observed when reducing the mesh size in the  $z$  direction.

**Dumbbell model.** In Fig. 1e, we plot the value of the critical height  $h_c$  as a function of the gap between neighbouring nanomagnets in two cases: within a full micromagnetic approach and using a dumbbell description. For the dumbbell description, we followed the procedure reported in ref. 29; we reproduced the results therein and present them in Extended Data Fig. 1, in which the ratio  $J_1/J_2$  is shown as a function of  $l/a$  and  $h/a$ , where  $l$  is the length of the nanomagnets (that is, the distance between the two magnetic charges) and  $a$  is the lattice parameter. The condition  $J_1 = J_2$  is indicated by the dark line.

**Sample fabrication.** The shifted artificial square ices were fabricated using a two-step electron-beam lithography process (Extended Data Fig. 2). The first step is dedicated to the design of the non-magnetic titanium/gold bases. Their shape was optimized to maximize the probability of successfully aligning the nanomagnets that were deposited in the second step. After exposing and developing a PMMA (poly(methyl methacrylate)) layer, the bases were deposited by electron-beam evaporation. To obtain a strong contrast in the scanning electron microscope through the PMMA resist, the top of the bases was made of a 50-nm-thick gold layer. The titanium thickness was then adjusted to obtain the desired height offset between the two sub-lattices. An ultrasound-assisted lift-off at  $80^\circ \text{C}$  in the remover revealed the bases. A new layer of PMMA resist was then spin-coated on the sample. Arrays of nanomagnets were patterned atop the base areas and deposited by electron-beam evaporation after developing the resist. The ferromagnetic layer was made of 30-nm-thick  $\text{Ni}_{80}\text{Fe}_{20}$  and a 3-nm-thick aluminium capping layer was deposited to avoid oxidation. A 5-nm-thick titanium layer between the bases and the permalloy layer was used to enhance its adherence. Finally, a similar lift-off process removed the unwanted material from the samples. For the two steps, a 150-nm-thick PMMA layer was spin-coated on a Si(100) substrate. Electron-beam lithography steps were done using a Raith LEO scanning electron microscope. The two layers were aligned manually in translation and rotation using adapted cross-marks. Our success rate using this method was around 20% for the nanomagnet sizes used here. Ti, Al, Au and  $\text{Ni}_{80}\text{Fe}_{20}$  were deposited with an evaporation rate of about  $0.1 \text{ nm s}^{-1}$  (pressure of  $10^{-5} \text{ mbar}$ ).

**Magnetic imaging.** Magnetic images were obtained using a NT-MDT magnetic force microscope. Custom-made low-moment magnetic tips were used to avoid magnetization reversal in the nanomagnets while scanning the arrays. The magnetic layer of the tips was made from a 30- or 50-nm-thick CoCr alloy.

**Demagnetization protocol.** Prior to their imaging, the samples were demagnetized using an in-plane oscillating field (250-mHz sine function) with decaying amplitude while in rotation at a typical frequency of several tens of hertz. A very slow field ramp was used to decrease the amplitude of the applied external magnetic field from 100 mT (well above the coercive field of our nanomagnets) to 0 in 72 h. As demonstrated by the magnetic configurations obtained on the different reference samples ( $h = 0$ ), our protocol efficiently brings the arrays within their low-energy manifold. In fact, our field protocols seem to be as efficient as the thermal annealing procedures used previously to capture the low-energy physics in square arrays of nanomagnets. It is possible that the free boundary conditions in our system, which contains several hundred nanomagnets, ease the demagnetization process by expelling high-energy configurations out of the lattice. However, several experimental observations suggest that the finite size of our arrays is not the key ingredient for the efficiency of the demagnetization protocol. First, we observe monopole defects close to the edges and in the core of the square lattice. There is no obvious sign that lattice edges ease the expulsion of monopoles. Second, contrary to most previous work, we use a very long demagnetization protocol (typically 72 h). The main reason for this is that the spin-spin correlations continue

to evolve even after several hours of demagnetization, consistent with what has been observed previously<sup>34,35</sup>. It seems that, in general, allowing a large number of spin-flip events is the key ingredient to reaching low-energy manifolds in artificial spin systems. For example, to demagnetize kagome lattices, 110-h demagnetization protocols helped us to reach an effective temperature of about  $0.06 J_{\text{nn}}$  (where  $J_{\text{nn}}$  is the nearest-neighbour coupling strength) and to observe spin fragmentation<sup>18</sup>. With shorter protocols, fragmentation was not observed because the associated (effective) temperature remained too high. For our square arrays, we find that three days is the optimum protocol length; we do not see substantial differences when applying longer demagnetization protocols.

**Numerical demagnetization.** To interpret our experimental data, we performed numerical simulations of the field demagnetization protocol. We consider a square array of magnetic point dipoles carrying a magnetic moment  $\mu$ . The interaction energy  $E_{ij}$  between two spins  $i$  and  $j$  separated by a distance  $r_{ij}$  is of dipolar-type, with a cut-off radius  $r_c$ :

$$E_{ij} = \begin{cases} \frac{1}{r_{ij}^3} \left[ \mu_i \cdot \mu_j - \frac{3}{r_{ij}^2} (\mu_i \cdot r_{ij})(\mu_j \cdot r_{ij}) \right] & \text{if } r_{ij} < r_c \\ 0 & \text{otherwise} \end{cases}$$

The local field  $H_{\text{loc}}^i$  felt by the dipole  $\mu_i$  is the sum of all dipolar fields coming from the surrounding spins plus the external applied magnetic field. Each dipole  $\mu_i$  behaves as an Ising pseudo-spin with its own switching field  $H_{\text{sw}}^i$ . Then, if

$$\frac{\mu_i}{\|\mu_i\|} \cdot H_{\text{loc}}^i > H_{\text{sw}}^i$$

the spin  $i$  is flipped. Following previous work<sup>22</sup>, we introduce a Gaussian distribution of the switching field  $H_{\text{sw}}^i$  to allow the system to approach its low-energy manifold. The probability  $P(H_{\text{sw}}^n)$  for a spin  $n$  to have a switching field  $H_{\text{sw}}^n$  is

$$P(H_{\text{sw}}^n) = \frac{1}{\sigma\sqrt{2\pi}} \exp \left[ -\frac{(H_{\text{sw}}^n - H_{\text{sw}})^2}{2\sigma^2} \right]$$

where  $H_{\text{sw}}$  is the average switching field and  $\sigma$  the spreading (standard deviation) of the distribution. For lattices with  $h = 0$  ( $h$  being the height offset), the ground state is ordered and  $\sigma$  provides a control on the density of nucleation sites during the demagnetization protocol. Our experimental results are well reproduced if  $\sigma$  is set to  $0.1 H_{\text{sw}}$ . In the simulations, the field ramp decreases linearly through  $10^6$  steps and  $10^4$  turns. Numerical demagnetizations showing the reversal of spin chains and the complete protocol are provided as Supplementary Videos 1 and 2. The same colour code is used here: the four vertex types (I–IV) are represented by squares coloured in blue, red, green and yellow, respectively. As in the experiments, type-IV vertices are never observed in the simulations.

**Magnetic structure factor.** We define the magnetic structure factor as in neutron scattering experiments, in which the spin correlations perpendicular to the diffusion vector  $\mathbf{q}$  are measured. We therefore define a perpendicular spin component  $S_{i\alpha}^\perp$ :

$$S_{i\alpha}^\perp = S_{i\alpha} - (\hat{\mathbf{q}} \cdot S_{i\alpha}) \hat{\mathbf{q}} \quad (1)$$

where  $\hat{\mathbf{q}}$  is the unit vector along the diffusion vector  $\mathbf{q}$ :

$$\hat{\mathbf{q}} = \frac{\mathbf{q}}{\|\mathbf{q}\|}$$

Extended Data Fig. 3a shows the geometric construction of the vectors involved in equation (1). The intensity  $I(\mathbf{q})$  scattered at location  $\mathbf{q}$  in reciprocal space is defined as

$$I(\mathbf{q}) = \frac{1}{N} \sum_{i,j=1}^{N/2} \sum_{\alpha,\beta=1}^2 S_{i\alpha}^\perp \cdot S_{j\beta}^\perp \exp(i\mathbf{q} \cdot \mathbf{r}_{i\alpha,j\beta}) \quad (2)$$

in which  $i$  and  $j$  scan all  $N/2$  unity cells, and  $\alpha$  and  $\beta$  the two sites of each cell. However, obtaining a more convenient form for equation (2) would enable a direct calculation starting from a magnetic configuration.  $I(\mathbf{q})$  can be split into two parts  $I = I^\parallel - I^\perp$  with

$$I^\parallel(\mathbf{q}) = \frac{1}{N} \sum_{\alpha,\beta=1}^2 g_\alpha(\mathbf{q}) g_\beta^*(\mathbf{q})$$

$$I^\perp(\mathbf{q}) = \frac{1}{N} \sum_{\alpha,\beta=1}^2 p_\alpha(\mathbf{q}) p_\beta^*(\mathbf{q})$$

where

$$g_{\alpha}(\mathbf{q}) = \sum_{i=1}^N \sigma_{i\alpha} \exp(i\mathbf{q} \cdot \mathbf{r}_{ij})$$

$$p_{\alpha}(\mathbf{q}) = \sum_{i=1}^N \hat{\mathbf{q}} \cdot \mathbf{S}_{i\alpha} \exp(i\mathbf{q} \cdot \mathbf{r}_{ij})$$

and  $\sigma_{i\alpha}$  is the Ising variable ( $\pm 1$ ) of the site ( $i\alpha$ ). In this split form,  $I$  is a real quantity. To compute  $I(\mathbf{q})$  diagrams in reciprocal space, we calculate the quantity  $I = g_1^2 + g_2^2 - (p_1 + p_2)^2$  at several  $\mathbf{q}$  locations. The magnetic structure factor reported in Extended Data Fig. 3b is composed of a matrix of  $120 \times 120$  points covering an area of  $q_x, q_y \in [-6\pi, 6\pi]$ . This area is 36 times larger than the first Brillouin zone.

**Generating low-energy magnetic configurations.** The magnetic structure factor of the square-ice model<sup>19</sup> was computed by averaging 1,000 low-energy spin configurations that satisfy the ice rule everywhere. To do so, we start from a magnetically saturated configuration and then flip a number  $N$  of randomly chosen spin loops. These loop flips are necessary to ensure that all of the generated spin configurations satisfy the ice rule. Because our lattice has free boundary conditions, the procedure leads to open (crossing the array) or closed loops (Extended Data Fig. 4). Both loops are used to generate a low-energy spin configuration. To decorrelate the initial (saturated) and final spin configurations, we take  $N$  to be of the order of the number of spins present in the array (840).

**Pinch points and correlation length.** The magnetic structure factor shown in Extended Data Fig. 3b is averaged over 1,000 ice-rule configurations. Pinch points located at the centre  $\Gamma$  of the Brillouin zone are clearly visible, indicating the existence of a Coulomb phase and algebraic spin–spin correlations, that is, a correlated, disordered magnet within which spin–spin correlations decay like point-dipole interactions<sup>36</sup>. The finite size of our arrays has consequences for the magnetic structure factor, in particular for the width of the pinch points. Extended Data Fig. 5 shows the influence of the lattice size  $L$  on the width of the pinch points, which narrow as the lattice size is increased. This width of the pinch points can be linked to a correlation length  $\xi$  in the system<sup>37</sup>. This correlation length can be extracted from a Lorentzian fit to the intensity profile passing through a pinch point:

$$I(\mathbf{q}) = A \frac{\xi^{-2}}{(q - q_0)^2 + \xi^{-2}} + B$$

where  $A$  and  $B$  are constants,  $q_0$  is the location of the pinch point in reciprocal space, and  $q$  is the diffusion vector. The correlation lengths deduced for different lattice sizes are reported in Extended Data Table 1. Uncertainties represent the variability within the 1,000 sampled spin states.

**Long-range dipolar interactions.** Although the square-ice model is a vertex model, here we have interacting dipoles with long-range effects. It is not clear whether the infinite range of the dipolar interaction affects the physics of the Coulomb phase. This question has been addressed in pyrochlore systems and is often referred to as the projective equivalence<sup>38</sup>, meaning that models of dipolar spin ice and nearest-neighbour spin ice are almost equivalent down to very low temperatures. However, as far as we know, this question has been addressed only to a small extent in two-dimensional square ice<sup>39</sup>. It has been shown numerically<sup>39</sup> that the Coulomb phase remains present down to low temperatures, even in the case of long-range dipolar interactions, and that the system eventually orders at very low temperatures. In our system, we envision two different magnetic orderings depending on the sign of  $h - h_c$ . For  $h < h_c$  we expect antiferromagnetic ordering (Fig. 1b), whereas for  $h > h_c$  we expect to see ferromagnetic lines in the system (Fig. 1c). But, similarly to spin-ice compounds and other artificial spin systems, reaching the ordered ground state is extremely difficult in practice, if not impossible. When we clearly observe the Coulomb phase, we have no indication of emerging magnetic order, which would indicate that our system could be described, to first order, by a short-range vertex model. This is in contrast to artificial kagome spin-ice systems in which the dipolar nature of the spin–spin interaction is clearly evidenced.

**Magnetic monopoles.** The monopoles we observe are very different from those described previously, from which two cases may be distinguished. In the first case, observation of monopoles in artificial square ice was achieved after saturating the arrays using a magnetic field applied along a (11)-like direction and by subsequently applying a field in the opposite direction with amplitude close to the coercive field of the system. The protocol then induced random nucleations of monopoles and triggered an avalanche process<sup>40</sup>. This protocol leads to unidirectional motion of the monopoles, which leave behind them chains of reversed spins often referred to as Dirac strings. Similar results have been obtained in thermally active arrays that have been magnetically saturated<sup>24</sup>. There, monopoles are metastable objects, created on purpose, embedded within a magnetically saturated state, that is, a spin configuration containing mainly type-II vertices (Fig. 4a). In the second case,

observation of monopoles in artificial square ice was achieved in arrays approaching the antiferromagnetic ordered ground state after being demagnetized or annealed<sup>24</sup>. These monopoles do not necessarily move along straight lines, but are always confined within a domain boundary that separates anti-phase ground-state domains made of type-I vertices (Fig. 4b). Moreover, these monopoles are not free particles, but topological defects that allow antiferromagnetic domains to grow; that is, they are charged objects embedded within a magnetically ordered state.

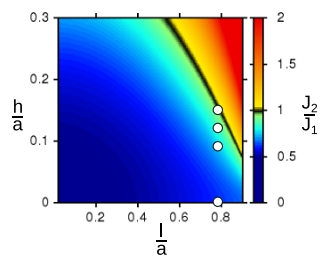
**Statistical ensemble.** To characterize the statistical ensemble of monopoles in the square-ice regime, we compared the mean value of the pairing length of the monopole/anti-monopole pairs (Extended Data Fig. 6) and the correlation length  $\xi$  deduced from the pinch-point analysis. We find that  $\xi = 4.4a$ , whereas the mean pairing length is about  $3a$ . These lengths are comparable and we can consider that the finite width of the pinch points is related to the presence of topological excitations within the Coulomb phase. Consequently, each monopole is expected to diffuse almost independently of its counterpart, allowing us to approximate each pair as two Ising domain walls propagating randomly within their one-dimensional chain—their classical Dirac string. Because domain walls are the source of decorrelation in a one-dimensional short-range Ising chain, we can extract an effective temperature  $T_{\text{eff}}/J_{\text{nn}}$  by fitting the mean pairing length to the correlation length of the one-dimensional Ising chain  $\xi = |\ln[\tanh(T_{\text{eff}}/J)]|$ , which gives  $T_{\text{eff}}/J \approx 1.15$ . This effective temperature should be taken with care and should not be used to show that our demagnetized samples are thermalized. Nevertheless, it is interesting that these quantitative values are compatible with one another as well as with classical Monte Carlo simulations of the associated spin model<sup>39</sup>.

**Thermally active square ice.** If the fabrication of thermally active, shifted square ice is the next step, the design we propose here might not be ideal as a way of accessing the superparamagnetic regime or in experiments that require high-temperature annealing. Using nanometre-thick nanomagnets could enable the superparamagnetic regime to be reached, but the surface of the Ti/Au bases we used might be too rough to allow the growth of a continuous, flat, nanometre-thick permalloy film. In addition, Ti and Au are probably not the best choice, because permalloy does not easily wet on them. For experiments that require thick films to be annealed above the Curie point of the ferromagnet, Ti and Au might again not be the right combination of materials because interdiffusion and dewetting might occur upon annealing at several hundreds of degrees Celsius. Simply because of these materials issues, our system needs to be optimized before being used to fabricate thermally active systems. Magnetic imaging is also challenging. Magnetic force microscopy is not the best technique with which to probe small amounts of material, especially in the superparamagnetic regime, because tip/sample interaction could affect the measurements. Photoemission electron microscopy is also difficult. One reason for this is that X-rays arrive on the sample at a  $16^\circ$  angle with respect to the surface, leading to shadowing effects in systems with important height profiles<sup>41–43</sup>. Even though photoemission electron microscopy can probe very small amounts of material, the geometry is not ideal for achieving magnetic contrast or accessing, for example, time evolution of spin-flip events in shifted square lattices.

**Data availability.** The datasets generated and analysed here are available from the corresponding author on reasonable request.

- Rougemaille, N. *et al.* Chiral nature of magnetic monopoles in artificial spin ice. *New J. Phys.* **15**, 035026 (2013).
- Zeissler, K. *et al.* The non-random walk of chiral magnetic charge carriers in artificial spin ice. *Sci. Rep.* **3**, 1252 (2013).
- Donahue, M. J. & Porter, D. G. *OOMMF User's Guide, Version 1.0*. Report No. NISTIR 6376 (National Institute of Standards and Technology, 1999).
- Wang, R. F. *et al.* Demagnetization protocols for frustrated interacting nanomagnet arrays. *J. Appl. Phys.* **101**, 09J104 (2007).
- Morgan, J. P., Bellew, A., Stein, A., Langridge, S. & Marrows, C. H. Linear field demagnetization of artificial magnetic square ice. *Front. Phys.* **1**, 28 (2013).
- Garanin, D. A. & Canals, B. Classical spin liquid: exact solution for the infinite-component antiferromagnetic model on the kagomé lattice. *Phys. Rev. B* **59**, 443–456 (1999).
- Fennell, T. *et al.* Magnetic Coulomb phase in the spin ice  $\text{Ho}_2\text{Ti}_2\text{O}_7$ . *Science* **326**, 415–417 (2009).
- Isakov, S. V., Moessner, R. & Sondhi, S. L. Why spin ice obeys the ice rules. *Phys. Rev. Lett.* **95**, 217201 (2005).
- Henry, L.-P. *Classical and Quantum Two-dimensional Ice: Coulomb and Ordered Phases*. <https://tel.archives-ouvertes.fr/tel-00932367/document> PhD thesis, Ecole normale supérieure de Lyon (2013).
- Phatak, C., Petford-Long, A. K., Heinonen, O., Tanase, M. & De Graef, M. Nanoscale structure of the magnetic induction at monopole defects in artificial spin-ice lattices. *Phys. Rev. B* **83**, 174431 (2011).
- Kimling, J. *et al.* Photoemission electron microscopy of three-dimensional magnetization configurations in core-shell nanostructures. *Phys. Rev. B* **84**, 174406 (2011).
- Da Col, S. *et al.* Observation of Bloch-point domain walls in cylindrical magnetic nanowires. *Phys. Rev. B* **89**, 180405 (2014).
- Jamet, S. *et al.* Quantitative analysis of shadow x-ray magnetic circular dichroism photoemission electron microscopy. *Phys. Rev. B* **92**, 144428 (2015).

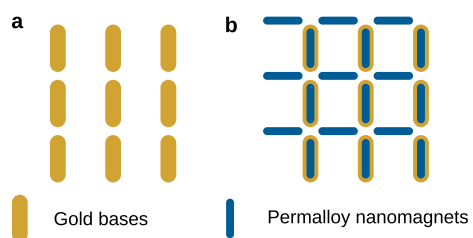




### Extended Data Figure 1 | Dumbbell description of the nanomagnets.

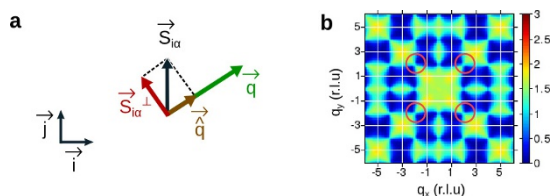
Map of  $J_1/J_2$  as a function of  $l/a$  and  $h/a$  for an isolated vertex.

The condition  $J_1 = J_2$  is indicated by the dark line. Our results perfectly reproduce those reported in ref. 29. The white dots indicate the values that correspond to the different samples studied here.

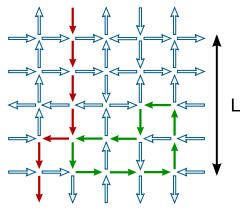


**Extended Data Figure 2 | Illustration of the two-step electron-beam lithography process.** **a**, Schematic of the gold bases subsequently used to shift the vertical sublattice. **b**, Schematic of the permalloy magnets on the vertical and horizontal sublattices.

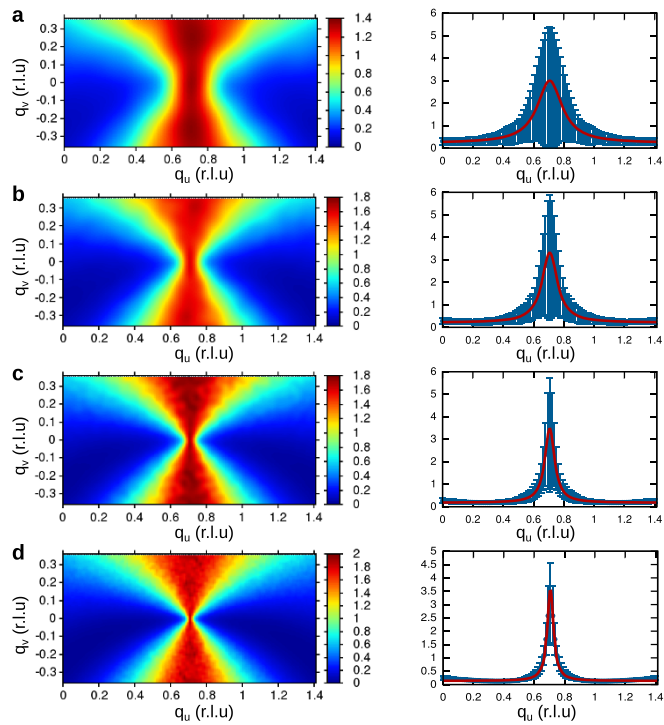




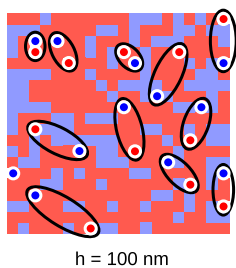
**Extended Data Figure 3 | Magnetic structure factor of the square-ice model.** **a**, Sketch of the vectors involved in equation (1). **b**, Magnetic structure factor for an ideal square-ice model, computed for 1,000 low-energy states made of  $N=840$  spins. Red circles indicate the regions of interest for the intensity profiles in Fig. 3f and Extended Data Fig. 5.



**Extended Data Figure 4 | Loop flips in the square lattice.** Schematic illustrating the open (red arrows) and closed (green arrows) spin loops used to generate a low-energy configuration that is representative of the massively degenerate ground-state manifold of the square-ice model<sup>19</sup>. The lattice contains 840 spins and the number of loops that are flipped between two decorrelated configurations is set to  $N = 840$ .  $L$  corresponds to the linear size of the square lattices.



**Extended Data Figure 5 | Analysis of the pinch points.** **a–d**, Maps of the pinch points indicated by red circles in Extended Data Fig. 3b (left) and associated intensity profiles along the  $q_v = 0$  direction (right), for different lattice sizes  $L$ :  $L = 10$  (**a**),  $L = 20$  (**b**),  $L = 40$  (**c**),  $L = 80$  (**d**). The colour scale refers to the intensity at a given point of reciprocal space. The coordinates  $(q_u, q_v)$  are relative to the intensity profile and do not correspond to the real axes of reciprocal space. The red curves are single-peaked Lorentzian fits; the points represent the mean and the error bars represent the standard deviation calculated from 1,000 random ice-rule configurations.



**Extended Data Figure 6 | Magnetic monopoles in artificial square ice.** Experimental spin configuration for  $h = 100 \text{ nm}$ . Type-I and -II vertices appear as blue and red squares, respectively. Monopoles appear as red and blue circles. Their associated pairing is represented by black ellipses.



Extended Data Table 1 | Correlation lengths extracted from the intensity profiles

$L$	10	20	40	80
$\xi$	$3.19a \pm 2\%$	$5.2a \pm 4\%$	$8.2a \pm 7\%$	$13a \pm 14\%$